MOA-2007-BLG-400 A Super-Jupiter-mass Planet Orbiting a Galactic Bulge K-dwarf Revealed by Keck Adaptive Optics Imaging

Aparna Bhattacharya[1,2], David P. Bennett[1,2], Jean Philippe Beaulieu[3,4], Ian A. Bond[5], Naoki Koshimoto[6,7], Jessica R. Lu[8], Joshua W. Blackman[4], Aikaterini Vandorou[4], Sean K. Terry[8], Virginie Batista[3], Jean Baptiste Marquette[3], Andrew A. Cole[4], Akihiko Fukui[9,10], Calen B. Henderson[11], and Clément Ranc[3]

[1] Code 667, NASA Goddard Space Flight Center, Greenbelt, MD 20771, USA; abhatta5@umd.edu
[2] Department of Astronomy, University of Maryland, College Park, MD 20742, USA
[3] UPMC-CNRS, UMR 7095, Institut d'Astrophysique de Paris, 98bis Boulevard Arago, F-75014 Paris, France
[4] School of Physical Sciences, University of Tasmania, Private Bag 37 Hobart, Tasmania 7001 Australia
[5] Institute of Natural and Mathematical Sciences, Massey University, Auckland 0745, New Zealand
[6] Department of Astronomy, The University of Tokyo, 7-3-1 Hongo, Bunkyo-ku, Tokyo 113-0033, Japan
[7] National Astronomical Observatory of Japan, 2-21-1 Osawa, Mitaka, Tokyo 181-8588, Japan
[8] University of California Berkeley, Berkeley, CA, USA
[9] Department of Earth and Planetary Science, Graduate School of Science, The University of Tokyo, 7-3-1 Hongo, Bunkyo-ku, Tokyo 113-0033, Japan
[10] Instituto de Astrofísica de Canarias, Vía Láctea s/n, E-38205 La Laguna, Tenerife, Spain
[11] NASA Exoplanet Science Institute, IPAC/Caltech, Pasadena, CA 91125, USA

Abstract

We present Keck/NIRC2 adaptive optics imaging of planetary microlensing event MOA-2007-BLG-400 that resolves the lens star system from the source. We find that the MOA-2007-BLG-400L planetary system consists of a $1.71 \pm 0.27 M_{\rm Jup}$ planet orbiting a $0.69 \pm 0.04 M_\odot$ K-dwarf host star at a distance of 6.89 ± 0.77 kpc from the Sun. So, this planetary system probably resides in the Galactic bulge. The planet–host star projected separation is only weakly constrained due to the close-wide light-curve degeneracy; the 2σ projected separation ranges are 0.6–1.0 au and 4.7–7.7 au for close and wide solutions, respectively. This host mass is at the top end of the range of masses predicted by a standard Bayesian analysis. Our Keck follow-up program has now measured lens-source separations for six planetary microlensing events, and five of these six events have host star masses above the median prediction under the assumption that assumes that all stars have an equal chance of hosting planets detectable by microlensing. This suggests that more massive stars may be more likely to host planets of a fixed mass ratio that orbit near or beyond the snow line. These results also indicate the importance of host star mass measurements for exoplanets found by microlensing. The microlensing survey imaging data from NASA's Nancy Grace Roman Space Telescope (formerly WFIRST) mission will be doing mass measurements like this for a huge number of planetary events.

Unified Astronomy Thesaurus concepts: Exoplanets (498); High-resolution microlensing event imaging (2138); Gravitational microlensing (672)

1. Introduction

Gravitational microlensing is unique in its ability to detect low-mass exoplanets (Bennett & Rhie 1996) beyond the snow line (Gould & Loeb 1992), where the formation of giant planets is thought to be most efficient (Lissauer 1993; Pollack et al. 1996). Observational results from microlensing have recently been used to constrain the distribution of planet-to-host star mass ratios, q, beyond the snow line and found a peak at roughly a Neptune mass (Suzuki et al. 2016). Recent results (Udalski et al. 2018; Jung et al. 2019), using a method somewhat similar to that of Sumi et al. (2010), have more precisely measured the location of this exoplanet mass ratio function peak and showed that the mass ratio function drops quite steeply below the peak.

A comparison of this observed mass ratio function (Suzuki et al. 2018) to the predictions of the core accretion theory as modeled by population synthesis calculations (Ida & Lin 2004; Mordasini et al. 2009) found a conflict between the smooth power-law mass ratio function observed at mass ratios of $>10^{-4}$ and the gap predicted by the runaway gas accretion process of the core accretion theory. This predicted mass ratio gap persisted independently of whether or not planetary migration was included in the population synthesis

calculations. This runaway gas accretion process has long been considered to be one of the main features of the core accretion scenario, but it had not been previously tested at orbital separations of a few astronomical unit. However, the development of the core accretion theory has largely focused on the formation of planets orbiting stars of approximately solar type, while exoplanet microlensing surveys study stars ranging from about a solar mass down to much lower masses, including late M-dwarfs and even brown dwarfs. So, it could be that the predicted exoplanet mass gap might still be seen for a sample of solar-type stars. This possibility can be tested by measuring the masses of the exoplanet host stars found by microlensing.

A complementary view of wide orbit exoplanet demographics can be obtained through a statistical analysis of radial velocity data. Fernandes et al. (2019) have recently argued that the distribution of gas giants peaks at semimajor axes of ~ 3 au for host stars of approximately solar type, and Wittenmyer et al. (2020) have found a flattening of the giant planet occurrence rate at $\gtrsim 1$ au with a smaller data set that is consistent with the Fernandes et al. (2019) results. While it is possible to constrain the distribution of exoplanets by combining planet detection methods that measure very different exoplanet attributes

(Clanton & Gaudi 2014a, 2014b), we can gain a much better understanding of exoplanet occurrence rates with better characterized exoplanet systems (Bennett et al. 2019), and this is what high angular resolution follow-up observations provide.

Measurements of the angular Einstein radius, θ_E, and the microlensing parallax amplitude, π_E, can each provide mass–distance relations (Bennett 2008; Gaudi 2012),

$$M_L = \frac{c^2}{4G}\theta_E^2\frac{D_S D_L}{D_S - D_L}; \; M_L = \frac{c^2}{4G}\frac{au^2}{\pi_E^2}\frac{D_S - D_L}{D_S D_L}. \quad (1)$$

D_L and D_S are distances to the lens and the source, respectively. These can be combined to yield the lens mass in an expression with no dependence on the lens or source distance,

$$M_L = \frac{c^2\theta_E\,au}{4G\pi_E} = \frac{\theta_E}{(8.1439\,\text{mas})\pi_E}M_\odot. \quad (2)$$

The angular Einstein radius can be measured for most planetary microlensing events because most planetary events have finite source effects that allow the measurement of the source radius crossing time, t_*. The angular Einstein radius is then given by $\theta_E = \theta_* t_E / t_*$, where t_E is the Einstein radius crossing time, and θ_* is the angular source radius, which can be determined from the source brightness and color (Kervella et al. 2004; Yoo 2004; Boyajian et al. 2014). As a result, the measurement of π_E for planetary events usually results in mass measurements. Unfortunately, the orbital motion of the Earth allows π_E to be determined for only a relatively small subset of events such as the ones that have very long durations (e.g., Gaudi et al. 2008; Bennett et al. 2010b), long duration events with bright source stars (e.g., Muraki et al. 2011), and events with special lens geometries (e.g., Sumi et al. 2016). The microlensing parallax program using the Spitzer space telescope at ∼1 au from Earth has recently expanded the number of events with microlensing parallax measurements (Udalski et al. 2015; Street et al. 2016), but recent studies indicate that systematic errors in the Spitzer photometry can affect some of the Spitzer π_E measurements (Dang et al. 2020; Gould et al. 2020; Koshimoto & Bennett 2020).

The method that can determine the masses of the largest number of planetary microlensing events is the detection of the exoplanet host star, as it separates from the background source star. This method uses an additional mass–distance relation obtained from a theoretical or an empirical mass–luminosity relation. The measurement of the angular separation between the lens and source stars provides the lens-source relative proper motion, μ_{rel}, which can be used to determine the angular Einstein radius, $\theta_E = \mu_{rel}t_E$. Due to the high stellar density in the fields where microlensing events are found, it is necessary to use high angular resolution adaptive optics (AO) or Hubble Space Telescope (HST) observations to resolve the (possibly blended) lens and source stars from other, unrelated stars. Unfortunately, this is not sufficient to establish a unique identification of the lens (and planetary host) star (Bhattacharya et al. 2017; Koshimoto et al. 2020), so it is necessary to confirm that the host star is moving away from the source star at the predicted rate (Batista et al. 2015; Bennett et al. 2015).

We are conducting a systematic exoplanet microlensing event high angular resolution follow-up program to detect and determine the masses of the exoplanet host stars with our NASA Keck Key Strategic Mission Support (KSMS) program (Bennett 2018), supplemented by HST observations (Bhattacharya et al. 2019b) for host stars that are most likely to be detected with the color-dependent centroid shift method (Bennett et al. 2006). This program has already revealed a number of microlens exoplanet host stars that are resolved from the source stars (Batista et al. 2015; Bennett et al. 2020a; Vandorou et al. 2020), and others that are still blended with their source stars, but show a significant elongation due to a lens-source separation somewhat smaller than the size of the point-spread function (PSF; Bennett et al. 2007, 2015; Bhattacharya et al. 2018).

Our follow-up program is midway through the analysis of the 30-event extended Suzuki et al. (2016) sample. We have mass measurements for 11 planets, so far, with the analysis of four more planetary events at an advanced stage. We have obtained upper or lower mass limits for two of these events, and we have data yet to be analyzed for 10 more events. This leaves only three planets from the Suzuki et al. (2016) that are not amenable to our mass measurement methods because their durations are too short for microlensing parallax measurements, and their source stars are too bright to allow for the detection of the planetary host stars. We are also beginning to expand our analysis into events from the MOA 9 yr retrospective analysis sample. This sample is expected to have about 60 planets, including planets like MOA-bin-1 (Bennett et al. 2012) in orbits so wide that they would not have a detectable microlensing signal from the star, were it not for the planet. It will also include planets in binary systems (Bennett et al. 2020b) that were excluded from the Suzuki et al. (2016) sample. Several mass measurements from this sample have already been published (Sumi et al. 2016; Beaulieu et al. 2017; Vandorou et al. 2020).

Our observing program is a pathfinder for the Nancy Grace Roman Space Telescope (formerly WFIRST) mission, which is NASA's next astrophysics flagship mission, to follow the James Webb Space Telescope. The Roman telescope (Spergel et al. 2015) includes the Roman Galactic Exoplanet Survey, based on the Microlensing Planet Finder concept (Bennett & Rhie 2002; Bennett et al. 2010a), which will complement the Kepler mission's statistical study of exoplanets in short-period orbits (Borucki et al. 2011; Thompson et al. 2018) with a study of exoplanets in orbits extending from the habitable zone to infinity (i.e., unbound planets). The microlens exoplanets discovered by Roman will not require follow-up observations because the Roman observations themselves will have high enough angular resolution to detect the lens (and planetary host) stars itself (Bennett et al. 2007). Our NASA Keck KSMS and HST observations and analysis will help us refine this mass measurement method and optimize the Roman exoplanet microlensing survey observing program.

The paper is organized as follows: Section 2 revisits the ground-based seeing-limited photometry data from 2007 and re-analyzes the light-curve modeling. Section 3 describes the details of our high-resolution follow-up observations and the reduction of the AO images. In Sections 4 and 5, we show the process of identifying the host star (which is also the lens) and the source star. In Section 5.2, we determine the geocentric relative lens-source proper motion from the lens and source identification and show that it matches with the prediction from the light-curve models. Finally in Sections 6 and 7, we discuss

Table 1
Best-fit Model Parameters

Parameter	$s < 1$	$s > 1$
t_E (days)	13.36 ± 0.38	13.39 ± 0.37
t_0 (HJD′)	4354.58111 ± 0.00005	4354.5310 ± 0.0083
u_0	-0.00026 ± 0.00009	-0.00425 ± 0.00080
s	0.366 ± 0.024	2.72 ± 0.14
α (rad)	-0.815 ± 0.034	-0.812 ± 0.030
$q \times 10^3$	2.39 ± 0.38	2.31 ± 0.28
t_* (days)	0.04711 ± 0.00008	0.04712 ± 0.00008
V_S	19.99 ± 0.03	19.99 ± 0.03
I_S	18.39 ± 0.03	18.39 ± 0.03
$\mu_{rel,G}$ (mas yr^{-1})	8.77 ± 0.13	8.77 ± 0.13
fit χ^2	3136.95	3136.86

the exoplanet system properties and the implications of its mass and distance measurement.

2. Revisiting Photometry and Light-curve Modeling

MOA-2007-BLG-400Lb was the eighth planet found by the microlensing method (Dong et al. 2009), located at R. A. $= 18 : 09 : 41.980$, decl. $= -29 : 13 : 26.95$, and Galactic coordinates $(l, b) = (2.3814, -4.7009)$. There have been improvements in light-curve photometry methods since the MOA-2007-BLG-400 discovery paper. The MOA team has learned to remove some potentially serious systematic photometry errors with a detrending method to remove systematic errors (Bennett et al. 2012), primarily from chromatic differential refraction. Bond et al. (2017) developed a variation of the Bond et al. (2001) photometry method that not only included detrending but also provides calibrated photometry. The MOA R_{moa} and V-band data, as well as the CTIO I and V band were re-reduced with the new method and calibrated to the Optical Gravitational Lensing Experiment (OGLE)-III photometry database (Szymański et al. 2011). This new method also produces photometry for images that may have one or two saturated pixels, and this seems to have added photometry for three I-band images that did not have photometry reported in Dong et al. (2009). However, this additional photometry does not appear to have a significant effect on the light-curve modeling. The CTIO H-band data were the difference image analysis (Bond et al. 2001) reduction from the discovery paper (Dong et al. 2009), but attempts to calibrate the CTIO H-band data were complicated by the unusual shape of the CTIO H-band PSFs. The reference frame DoPhot photometry (Schechter et al. 1993) we obtained for these images was unreliable, with many false "stars" detected due to irregularities in the H-band PSFs of the CTIO SMARTS ANDICAM images.

Because of this change in photometry, we redid the light-curve modeling for this event. This was done using the Bennett (2010) modeling code, and the resulting model parameters are given in Table 1. The model parameters that are in common with single-lens events are the Einstein radius crossing time, t_E, the time, t_0, and distance, u_0, of closest alignment between the source and the lens center-of-mass, where u_0 is given in units of the Einstein radius. There are four additional parameters for binary lens systems: the star–planet separation in Einstein radius units, s, the angle between the lens axis and the source trajectory, α, the planet–star mass ratio, q, and the source radius crossing time, t_*, which is needed for events, like most

planetary events, that have very sharp intrinsic light-curve features that resolve the angular size of the source star. The brightness of the source star, f_{Si} and blended stars, f_{Bi} are also fit to the observed brightness for each passband, i, using the formula $F_i(t) = f_{Si} A(t) + f_{Bi}$, where $A(t)$ is the magnification from the model, and $F_i(t)$ is the observed flux in the ith passband. Because this is a linear equation, f_{Si} and f_{Bi} can be solved exactly for each model in the Markov Chain (Rhie et al. 1999). For each data set that has been calibrated, the f_{Si} values are used to determine the calibrated source brightness.

As discussed by Dong et al. (2009), this event has degenerate close and wide separation light-curve models with nearly identical best-fit χ^2 values. The main changes in our model parameters compared to the Dong et al. (2009) discovery paper are that (1) the Einstein radius crossing time, t_E, has decreased by about 7%, which is just over 2σ, and (2) the planetary mass ratio, q has decreased by 8%, which is $\sim 0.6\sigma$. The change in t_E is due to the change in the MOA photometry, which affects the light-curve shape at low magnification. Then, the change in the mass ratio, q, may be attributed to the fact that $q t_E$ is an invariant (Yee et al. 2012). Our final results are determined from a set of six Markov Chain Monte Carlo (MCMC) runs with a total of 263,000 light-curve models. The new light-curve peak is shown in Figure 1, which can be compared to Figures 1 and 2 of Dong et al. (2009), which show that the new photometry and models are very similar to the Dong et al. (2009) photometry and models.

Another improvement in our analysis is the measurement of the lens-source relative proper motion, $\mu_{rel,G} = 8.79 \pm 0.18$ mas yr^{-1}. The G suffix refers to the use of the inertial Geocentric reference frame that moves with the velocity of the Earth at the time of the event. This new measurement compares to $\mu_{rel,G} = 8.0 \pm 0.46$ mas yr^{-1} as reported in Dong et al. (2009). There are several ingredients to this improvement. The improved MOA and CTIO photometry provides more accurate t_E and color values, and the analysis of Boyajian et al. (2014), as optimized for microlensing targets (Bhattacharya et al. 2016), provides a more accurate source radius. Finally, Nataf et al. (2013) has provided a more accurate determination of the properties of the red clump giants that are used to determine the dust extinction in the foreground of the source. The light-curve measurement of $\mu_{rel,G}$ is based on the planetary signal, and its consistency with our measurement of the lens-source separation can be considered to be a confirmation of the original planetary interpretation of the light curve (Bennett et al. 2015; Batista et al. 2015).

3. Follow-up Observations

The list of all Keck observations and their exposures is listed in Table 2.

3.1. Wide Camera

The event was observed with the Keck AO NIRC2 (Wizinowich et al. 2000) instrument during the early morning of 2018 August 3 as part of our Keck NASA KSMS program. Eight dithered exposures, each of 30 s, were taken in the K_S short passband with the wide camera. In this paper, from now on we refer to the K_S band as the K band. Each wide camera image covers a 1024×1024 square pixel area, and each pixel size is about 39.686×39.686 mas^2. These images were flat field and dark current corrected using standard methods, and
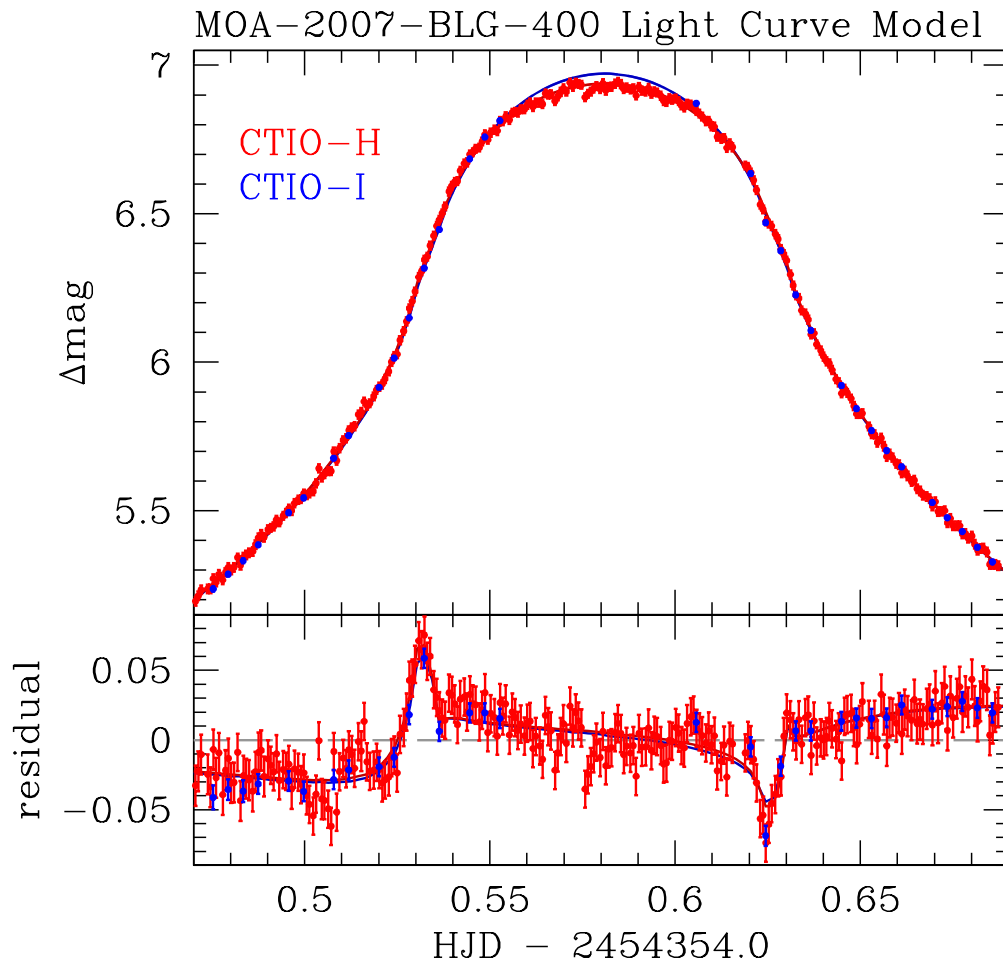
Figure 1. The MOA-2007-BLG-400 light-curve peak observed in the *H* and *I* bands from the SMARTS Telescope at CTIO. The top panel shows the light-curve peak with different light curves for the *H* and *I* bands in red and blue, respectively. The light curve is color dependent due to limb darkening. The planetary signal reaches a maximum amplitude of 0.06 mag compared to the best-fit single-lens light curve, but these deviations occur when the stellar limb crosses the central caustic and the magnitude changes most rapidly. Therefore, it is much easier to see the planetary signal in the residuals from the best-fit single-lens light curve shown in the bottom panel.

Table 2
Keck Observations

Date of Obs.	Band	Camera	Exposure Time (s)	Number of Exposures
2013 Jul 18	*H*	Wide	30	10
2013 Jul 18	*H*	Narrow	60	1
2018 Aug 3	*K*	Wide	30	8
2018 Aug 3	*K*	Narrow	60	11
2018 Aug 6	*H*	Narrow	60	17

then stacked using the SWarp Astrometics package (Bertin et al. 2002). The details of our methods are described in Batista et al. (2014). We used an aperture photometry method on these wide images with SExtractor software (Bertin & Arnouts 1996). These wide images were used to detect and match 57 bright isolated stars to the VISTA Variables in the Via Lactea (VVV) public survey catalog (Minniti et al. 2010) for calibration purposes. The same event was also observed with the wide camera on 2013 July 18 in the *H* band. There are 10 wide camera images. These images were reduced and stacked using the same method used for the *K* band. The average FWHM of this wide camera stack image is 110 mas. Fifty-nine bright isolated stars were used from the *H*-band stack image to

calibrate to VVV. Note that, in both the 2013 and 2018 wide camera images, the lens and source were not resolved. As a result, we need NIRC2 narrow camera images to resolve and to identify the lens system.

3.2. Narrow Camera

This event was also observed on 2018 August 3 with the Keck NIRC2 narrow camera in the *K* band using laser guide star adaptive optics. The main purpose of these images is to resolve the lens host star from the source star. Eleven dithered observations were taken with 60 s exposures. The images were taken with a small dither of $0\rlap{.}''7$ at a position angle (P.A.) of 0° with each frame consisting of four co-added 15 s integrations. The overall FWHM of these images varied from 82 to 98 mas. For the reduction of these images, we used *K*-band dome flats taken with the narrow camera on the same day as the science images. There were five dome flat images with the lamp on and five more images with the lamp off, each with 60 s exposure time. Also, at the end of the night, we took 10 sky images using a clear patch of sky at an (R.A., decl.) of (20:29:57.71, −28:59:30.01) with an exposure time of 30 s each. All of these images were taken with the *K*-band filter. These images were used to flat field, bias subtract, and remove bad pixels and

cosmic rays from the 11 raw science images. The strehl ratio of these clean images varied over the range 0.21–0.41. Finally these clean raw images were distortion corrected, differential atmospheric refraction corrected, and stacked into one image. We used that for the final photometry and astrometry analysis.

On 2018 August 6, we observed this event again with the NIRC2 narrow camera, but this time in the H band. We adopted an observation strategy similar to the K-band exposures. Seventeen dithered H-band observations were taken with 60 s exposures. Each exposure consisted of three co-added 20 s integrations. The H-band images were also taken with a small dither of 0.″7 at a P.A. of 0°. The overall FWHM of these images varied from 64 to 76 mas. We also took 10 H-band dome flats with the narrow camera—five with lamp on and the other five with the lamp off. We took 15 frames of sky observations by imaging the clear patch of sky at an (R.A., decl.) of (20:29:57.71, −28:59:30.01). Following the method mentioned for the K band, the 17 raw science images were cleaned using the calibration images and were stacked into one image. The strehl ratio of these clean images varied over the range 0.12–0.19. Both the K-band and H-band clean images were distortion corrected and stacked using the methods of Lu (2008), Service et al. (2016), and Yelda et al. (2010). Note that, even though the average FWHM of the H-band images is smaller than that of the K-band images, the strehl ratios are significantly worse for the H-band images. This is typically the case for wavelengths shorter than the K band with the current AO systems on the Keck telescopes and other 8–10 m class telescopes.

There are 1024×1024 pixels in each narrow camera image with each pixel subtending 9.942 mas on each side. Since the small field of these narrow images covers only a few bright stars, it is difficult to directly calibrate them to VVV, so we use the wide camera K and H stack images that were already calibrated to VVV to calibrate the narrow camera images. This gives us the brightness calibration between the stacked narrow camera image to the VVV image. The photometry used for the narrow camera image calibration is from DAOPHOT analysis (Section 4).

There were also four H-band images (each of 60 s) of this same event taken on 2013 July 18 using the Keck NIRC2 narrow camera. Out of these four images, only one image has a reasonably good signal-to-noise ratio (S/N). The other two images have poor S/Ns, probably due to the cloudy weather. In the last image, the target was outside the frame. Due to the lack of sky images, we could not use the method of Lu (2008), Service et al. (2016), and Yelda et al. (2010) to reduce this image. The only good image has an FWHM of 94 mas. We analyzed this image directly with DAOPHOT. This analysis was used to confirm our identification of the host (and lens) star by showing that the candidate lens star matches the motion predicted by the light-curve model between the 2013 and 2018 observations (see Section 5.3).

4. Keck Narrow Camera Image Analysis

4.1. 2018 Narrow Data

In this section, we use DAOPHOT (Stetson 1987) to construct a proper empirical PSF model to identify the two stars (the lens and the source) in the narrow stack images. We started our analysis with the 2018 Keck narrow camera images. We used the same method as Bhattacharya et al. (2018) to build

PSF models for both the K- and H-band narrow camera stack images. We built these PSF models in two stages. In the first stage, we ran the FIND and PHOT commands of DAOPHOT to find all of the possible stars in the image. In second stage, we used the PICK command to build a list of bright ($K < 18.5$) isolated stars that can be used for constructing our empirical PSF model. Our target object was excluded from this list of PSF stars because it is expected to consist of two stars that are not in the same position. From this list of stars, we selected the four nearest stars to the target that had sufficient brightness, and we built our PSF model from these stars. We chose only the nearest stars in order to avoid any effect of PSF shape variations across the image. We used the same PSF stars for both the K- and H-band data sets.

Once we built the PSF model, we fit all of the stars with this model. This step produced the single-star residual fit for the target that is shown in Figure 2(C). Inspection of this residual image from the single-star fit indicates that there is an additional star near the target object. So, we tried fitting the region of the target object with a two-star model. The two-star fits produced a smoother residual than the single-star fit, as shown in Figure 2. The results of these dual-star fits are given in Tables 3 and 4. Both the single-star and dual-star fits were done using the Newton–Raphson method of standard DAOPHOT. As we discuss in Section 5, we identify the brighter of the two stars as the source for the MOA-2007-BLG-400 microlensing event, and the fainter star to the east as the lens and planetary host star.

4.2. Error Bars from the Jackknife Method

We have developed a new method of error bar determination using the Jackknife method (Quenouille 1949, 1956; Tukey 1958; Tierney & Mira 1999). This method is able to measure the variance due to the PSF variations in the individual images. In this method, if there are N clean images, then N new stack images are built by excluding one of the N images from each new stack. Hence, each of these N stacks consists of $N-1$ images. Then, these N images are analyzed with DAOPHOT to build empirical PSFs for each stack image. The four nearby stars used to build the empirical PSF model for the full stack of N images are used to build the empirical PSFs for these jackknife stack images of $N-1$ images. Next, the target in each image is fitted with the dual-star PSF models. We built an automated code that runs the image reduction method from Service et al. (2016) and Yelda et al. (2010) and DAOPHOT routines to make these N combinations. Once we have these N combinations, we perform statistics of a parameter on these N stacked images made from $N-1$ images instead of one stacked image made from N images. The standard error of a parameter x in Jackknife is given by:

$$\mathrm{SE}(x) = \sqrt{\frac{N-1}{N} \sum (x_i - \bar{x})^2}. \qquad (3)$$

The x_i represents the value of the parameter measured in each of the combined images, and $\bar{x}$ represents the mean of the parameter x from all of the N stacked images. This Equation (3) is the same formula as the sample mean error, except that it is multiplied by $\sqrt{N-1}$.

We ran our automated code on 2018 K- and H-band images to build 11 K-band stacks of 10 combined images and 17 H-band stacks of 16 combined images, respectively. To build
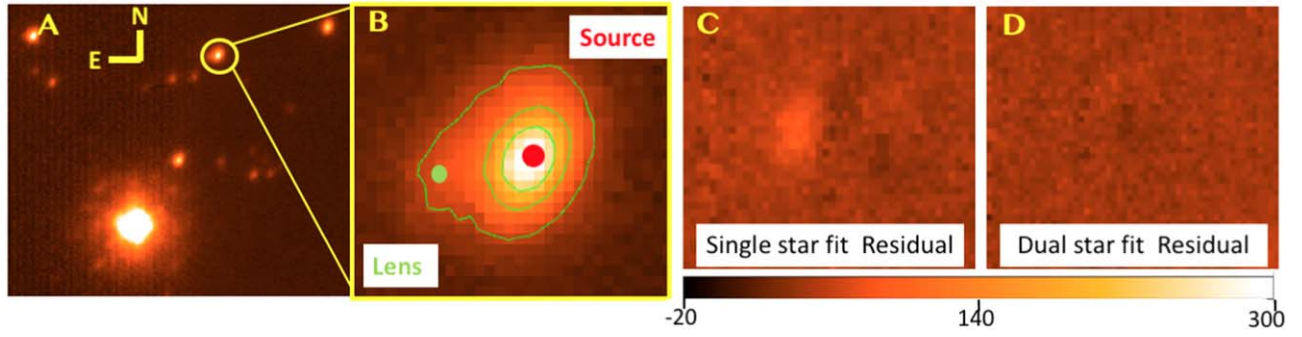
Figure 2. Panel (A): a $4'' \times 3''$ section of the stack image of 11 Keck K-band images, taken with the narrow camera, with the yellow circle indicating the target. Panel (B): a $0''.4 \times 0''.3$ close-up the target object. The source and lens positions are obtained from the best-fit dual-star PSF model. Panel (C): the residual image after subtracting the best-fit single-star PSF model. The residual shows a clear indication of the presence of an additional star east of the target. Panel (D): the residual image after subtracting the best-fit dual-star PSF model. This shows a smooth residual, confirming the second star at a separation of ∼96 mas. Panels (C) and (D) use the same photometry scale.

Table 3
Measured Source and Lens Photometry and Astrometry from 2018 data

| Passband | Calibrated Magnitudes | | Separation (mas) | | | |
	Source	Lens	East	North	Total	Angle (deg)
Keck K	16.43 ± 0.04	18.93 ± 0.08	93.3 ± 1.6	-22.8 ± 1.9	96.04 ± 2.48	103.73 ± 0.56
Keck H	16.58 ± 0.04	19.08 ± 0.11	91.8 ± 2.5	-27.9 ± 2.4	95.95 ± 3.46	106.91 ± 0.71

Note. The separation was measured 10.894 yr and 10.903 yr after the peak of the event in the K and H bands, respectively. The angle is calculated with respect to north.

Table 4
Measured Lens-source Relative Proper Motion

| Passband | $\mu_{\rm rel,H}$(mas yr^{-1}) | | $\mu_{\rm rel,H}$(mas yr^{-1}) | |
	East	North	galactic-l	galactic-b
Keck K	8.56 ± 0.15	-2.09 ± 0.17	2.26 ± 0.17	-8.52 ± 0.16
Keck H	8.43 ± 0.23	-2.56 ± 0.19	1.79 ± 0.21	-8.63 ± 0.22
Mean	8.52 ± 0.13	-2.29 ± 0.13	2.07 ± 0.13	-8.55 ± 0.13

these stacks, our image reduction pipeline chooses the image with lowest FWHM as the reference image. However, there was one stack in both the K and H passbands where this reference image is removed. In that case, the image with the lowest FWHM among that sample was automatically selected as the reference image. For the stack images that were built with the same reference image, the star coordinates were similar, and there was no need to run the FIND and PICK commands in DAOPHOT. For the stack image that had a different reference frame, the star pixel coordinates were shifted, and we had to double-check by eye that indeed the same PSF stars were selected. Once the stack images were analyzed using DAOPHOT to build empirical PSFs and fit dual-star models, the error bars on lens-source separations and fluxes were calculated following Equation (3). We noticed that the H-band residual of the fits were not as smooth as the K-band fit. The H-band χ^2 for the dual-star fit is 4.39 times higher than the K-band χ^2 for the same size of fitting box. As a result, we rescale the H-band error bars via multiplying them by $\sqrt{4.39} = 2.09$. These error bars are reported in Table 3. The error bars in Table 4 are based on the error bars in Table 3 because the Heliocentric lens-source relative proper motion, $\mu_{\rm rel,H}$, is proportional to the lens-source separation.

The running time for this software on 11 images was about 1 hr, and 17 images took about 1.5 hr on a quad core i7 CPU with 16 GB RAM. This shows that this method is not too time consuming, and it can be easily run for 70 images over a few days. Since our largest data set for a single event is ≈70 images, this indicates that this jackknife method can be used for all of the events we observe in this program.

4.3. 2013 Narrow Camera Data

We ran the DAOPHOT analysis on the single high-quality 2013 H-band image using the same method as for 2018 data. We used four PSF stars to build the empirical PSF model and run a dual-star fit. With only a single image, we obviously cannot use the jackknife method to estimate the position error bars. However, we expect the same image PSF variance as we saw in the 2018 H-band data. So, we take the 2018 H-band position errors and multiply them by $\sqrt{17}$ to account for the 17 images contributing to the 2018 result compared to the single 2013 image. This yields an offset between the faint and bright stars of 59.5 ± 10.4 mas east and -4.5 ± 9.0 mas north. The positions of the stars that we identify as the lens and source are shown in Figure 3 for both the 2013 and 2018 measurements. The 2013 analysis indicates that the H-band magnitudes of the source and the fainter stars are 16.61 ± 0.04 and 19.01 ± 0.11, respectively. This is consistent with the 2018 H-band magnitudes of 16.58 ± 0.04 and 19.08 ± 0.11, respectively. These measurements were solely used to confirm that the lens motion is consistent over time.

5. Interpreting Our Keck Results

In the preceding sections, we have referred to the Keck images of the source and lens (and planetary host) stars. Now, we discuss the analysis that shows that our identifications of the
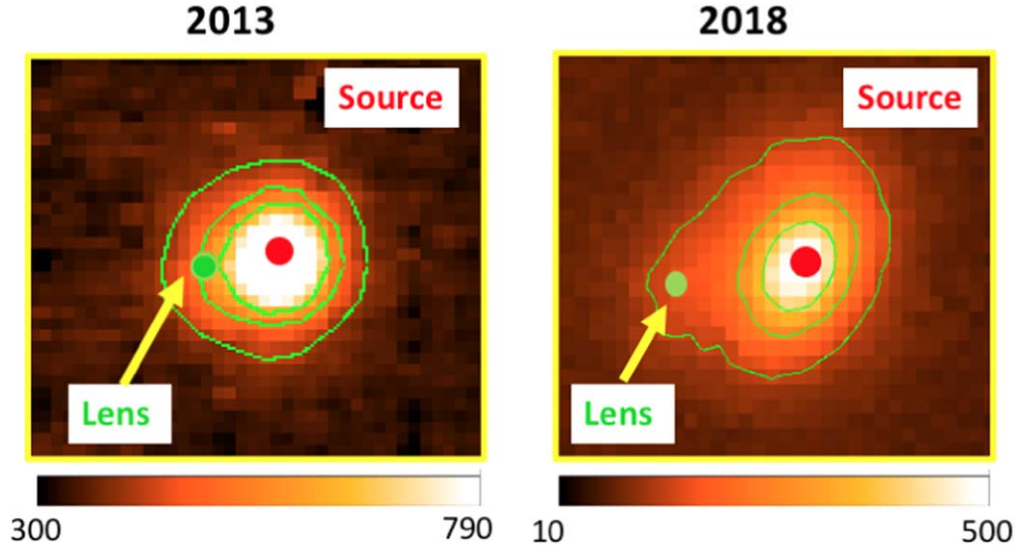
Figure 3. These images show the positions for the stars that we identify as the source and lens in a 2013 *H*-band image (left) and a 2018 *K*-band stack image. The lens star is 59.5 ± 10.4 mas east and -4.5 ± 9.0 mas north of the source in the 2013 *H*-band image. A comparison with a combined 2018 Keck *K* image is shown on the right, where the lens is measured to be 93.3 ± 1.6 mas east and -22.8 ± 1.9 mas north of the source. Both images are presented with east to the left, and north up. The Keck 2018 image is a combined image based on 11 frames, whereas the 2013 image is our single high-quality image from 2013. As discussed in Section 5.3, the 2013 lens-source relative proper motion is consistent with the 2018 lens-source relative proper motion at $<1\sigma$ in both the east and north directions.

source and lens stars are correct. For a high-magnification event, like MOA-2007-BLG-400, it is possible to determine the position of the lens and source stars at the time of the event to a precision of better than 20 mas based on the MOA difference images when the source was highly magnified. This precision might be slightly degraded by the coordinate transformation between the MOA images and the Keck NIRC2 wide camera images, but this analysis, based on the 2013 *H*-band wide images, uniquely identifies the target star. Later, we identify the target in the 2018 Keck narrow images based on the identification in the 2013 Keck wide images. This target star is shown by the yellow circle in Figure 2(A).

5.1. Confirming the Source Star Identification

Our reanalysis of the light-curve model of this event (with improved MOA and CTIO photometry) showed the best-fit model (wide) gives a source brightness of $I_S = 18.38 \pm 0.03$ and $V_S = 19.98 \pm 0.03$. The average extinction and reddening of the red clump stars within $2'.5$ of the target are $A_I = 0.92$ and $E(V - I) = 0.75$, as calculated from the OGLE-III photometry catalog (Szymański et al. 2011). This means the source color is $(V - I)_S = 1.61 \pm 0.04$, and the extinction-corrected color is $(V - I)_{S,0} = 0.86 \pm 0.04$. From the color–color relation of Kenyon & Hartmann (1995), $(V - I)_{S,0} = 0.86$ corresponds to the dereddened colors of $(I - H)_{S,0} = 1.03$ and $(I - K)_{S,0} = 1.11$. So the extinction-corrected source brightnesses in K and H bands are $K_{S,0} = 16.35 \pm 0.06$ and $H_{S,0} = 16.43 \pm 0.06$, respectively, including a 5% uncertainty in the color–color relation. This implies the dereddened color $(H - K)_{S,0} = 0.08$. From Cardelli et al. (1989), the extinctions in the K and H bands are $A_K = 0.13$ and $A_H = 0.21$ at 6.9 kpc, respectively (see Section 6). Hence, the expected K-band and H-band calibrated magnitudes of the source are $K_S = 16.48 \pm 0.06$ and $H_S = 16.64 \pm 0.06$, respectively.

The dual-star fits to 2018 narrow camera Keck images imply that the two stars located at the position of the target are resolved. The best dual-star fit yielded two stars with calibrated K magnitudes of 16.43 ± 0.04 and 18.93 ± 0.08. The H

magnitudes for those same stars are 16.58 ± 0.04 and 19.08 ± 0.11. The error bars are calculated using the jackknife method, as discussed in Section 4.2. The brighter star from these dual-star fits matches the expected source magnitudes derived above. Hence, we identify the brighter star as the source star and the fainter star as the potential lens star.

5.2. Determination of Relative Lens-source Proper Motion

We will determine the relative proper motion between the lens candidate and the source star. In the this subsection, we will measure the heliocentric relative proper motion from narrow Keck images and then transform that to geocentric frame. Then we will compare the measured geocentric relative proper motion to the predicted relative lens-source proper motion from the light curve. This will help us to confirm that the second star is indeed the lens star later. Since in the next section we show that this possible lens star is the lens, we will call the relative proper motion the relative lens-source proper motion hereafter, for simplicity.

The source and the fainter star are separated by slightly more than the FWHM of the 2018 *H*- and *K*-band images, and the measured separation can be used to compute the lens-source relative proper motion, μ_{rel}, which can be compared with the μ_{rel} prediction from the light curve. However, this issue is complicated by the fact that the lens-source separation measurements determine the relative proper motion in a Heliocentric frame, $\mu_{rel,H}$, while the light curve measures the relative proper motion in an inertial Geocentric reference frame, $\mu_{rel,G}$, which moves with the Earth's velocity at the time of the event. The relationship between these reference frames is given by Equation (4), but for most events, and especially for events like MOA-2007-BLG-400, where a distant lens is favored, we have $\mu_{rel,H} \approx \mu_{rel,G}$ to a good approximation.

Our high-resolution observations of 2018 were taken $\sim$10.9 yr after the microlensing event magnification peak. If these images were taken exactly 11 yr after the microlensing magnification, then we would not need to consider the relative position of the Earth with respect to the Sun when determining

the heliocentric lens-source relative proper motion from the separation measured from the Keck images. The Earth was displaced 0.6 au between the time of the event magnification peak and the Keck observations. With a lens distance of 6.89 kpc (see Section 6), this implies an angle of ~0.09 mas, which is $\ll 1\sigma$ of the separation measurement uncertainties given in Table 4. Therefore, we are safe in neglecting this effect for our Keck measurement of the relative proper motion in the Heliocentric reference frame, $\boldsymbol{\mu}_{\mathrm{rel,H}}$.

At the time of peak magnification, the separation between lens and source was $\sim|u_0\theta_{\mathrm{E}}| \sim 0.001$ mas. Hence, by dividing the measured separation by the time interval of 10.894 yr (for the K band or 10.903 yr for the H band), we obtain the heliocentric lens-source relative proper motion, $\boldsymbol{\mu}_{\mathrm{rel,H}}$. A comparison of these values from our independent dual-star fits for the H and K bands is shown in Table 4, where error bars are estimated from the jackknife method. In Galactic coordinates, the mean $\boldsymbol{\mu}_{\mathrm{rel,H}}$ components are $\mu_{\mathrm{rel,H},l} = 2.07 \pm 0.13$ mas yr^{-1} and $\mu_{\mathrm{rel,H},b} = -8.55 \pm 0.13$ mas yr^{-1}, with an amplitude of $\mu_{\mathrm{rel,H}} = 8.80 \pm 0.18$ mas yr^{-1} at an angle of $\sim-74°$ from the direction of Galactic disk rotation. The dispersion in the motion of stars in the bar-shaped bulge at the lens distance of $D_{\mathrm{L}} \approx 6.97$ kpc (as presented in Section 6) is about ~2.5 mas yr^{-1} in each direction. The source is also in the bulge at about ~8 kpc, where a similar dispersion in the motion of stars is expected. The relative proper motion is the difference of two proper motions, so the average difference in proper motion is the quadrature sum of four ~2.5 mas yr^{-1} values or ~5 mas yr^{-1}. However the microlensing rate is proportional to μ_{rel}, so the average μ_{rel} is greater than >5 mas yr^{-1}. So, our measured $\boldsymbol{\mu}_{\mathrm{rel,H}}$ value is only slightly higher than the typical value for bulge–bulge lensing events.

We also calculate the heliocentric relative lens-source proper motion from 2013 Keck narrow image. We find a lens-source separation of 59.5 ± 10.4 mas to the east and -4.5 ± 9.0 mas to the north. Dividing by the 5.83 yr interval between the microlensing event peak and the 2013 Keck observations, we find $(\mu_{\mathrm{rel,H,E}},\ \mu_{\mathrm{rel,H,N}}) = (10.2 \pm 1.8,\ -0.8 \pm 1.5)$ mas yr^{-1}. This is consistent with the relative lens-source proper motion measured from 2018 Keck narrow data within 1σ error bars.

Our light-curve models were done in a geocentric reference frame that differs from the heliocentric frame by the instantaneous velocity of the Earth at the time of peak magnification, because the light-curve parameters can be determined most precisely in this frame. However, this also means that the lens-source relative proper motion that we measure with follow-up observations is not in the same reference frame as the light-curve parameters. This is an important issue because, as we show below (see Section 6), the measured relative proper motion can be combined with the brightness of the source star to determine the mass of the lens system. The relation between the relative proper motions in the heliocentric and geocentric coordinate systems is given by Dong et al. (2009):

$$\boldsymbol{\mu}_{\mathrm{rel,H}} = \boldsymbol{\mu}_{\mathrm{rel,G}} + \frac{\boldsymbol{v}_{\oplus}\pi_{\mathrm{rel}}}{\mathrm{au}}, \qquad (4)$$

where $\boldsymbol{v}_{\oplus}$ is the projected velocity of the Earth relative to the Sun (perpendicular to the line of sight) at the time of peak magnification. The projected velocity for MOA-2007-BLG-400 is $\boldsymbol{v}_{\oplus\mathrm{E,\ N}} = (6.9329, -2.8005)$ km s^{-1} = $(1.46, -0.59)$ au yr^{-1} at the peak of the microlensing. The relative parallax is defined

as $\pi_{\mathrm{rel}} \equiv (1/D_{\mathrm{L}} - 1/D_{\mathrm{S}})$, where D_{L} and D_{S} are the lens and source distances, respectively. Hence Equation (4) can be written as:

$$\boldsymbol{\mu}_{\mathrm{rel,G}} = \boldsymbol{\mu}_{\mathrm{rel,H}} - (1.46, -0.59) \times (1/D_{\mathrm{L}} - 1/D_{\mathrm{S}}). \qquad (5)$$

Since $\boldsymbol{\mu}_{\mathrm{rel,H}}$ is already measured in Table 4, Equation (4) yields the geocentric relative proper motion, $\boldsymbol{\mu}_{\mathrm{rel,G}}$ as a function of the lens distance. Now at each possible lens distance, we can use the $\boldsymbol{\mu}_{\mathrm{rel,G}}$ value from Equation (5) to determine the angular Einstein radius, $\theta_{\mathrm{E}} = \mu_{\mathrm{rel,G}} t_{\mathrm{E}}$. Since we already know the θ_{E} value from the light-curve models, we can use that here to constrain the lens distance and relative proper motion. Using this method, we determined the vector relative proper motion to be $\boldsymbol{\mu}_{\mathrm{rel,G}}(E, N) = (8.49 \pm 0.14, -2.28 \pm 0.14)$, and the magnitude of this vector is $\mu_{\mathrm{rel,G}} = 8.79 \pm 0.18$. This value is consistent with the predicted $\mu_{\mathrm{rel,G}} = 8.87 \pm 0.54$ mas yr^{-1} from the light-curve models.

5.3. Confirmation of the Host Star Identification

The simplest μ_{rel} comparison is to compare the measured relative proper motions in the 2018 and 2013 Keck observations. As shown in the preceding subsection, these values are each within 1σ of the mean $\mu_{\mathrm{rel,H}}$ values reported in Table 4. This consistency implies that both the 2013 and 2018 measurements are consistent with the same lens-source relative motion and with the lens and source being in the same position at the time of the microlensing event.

These analyses completely rule out the possibility of the additional star being a source companion. If this additional star was a companion to the source, it would be co-moving with the source and would not move away from the source. Hence, the motion between 2013 and 2018 is inconsistent with a star bound to the source. An unrelated star in the bulge would have to mimic the proper motion of the lens star, and the probability of this is $<0.06\,\%$ according to an analysis using the method of Koshimoto et al. (2020). There is also the possibility that we have detected a binary companion to the lens instead of the lens star. This possibility is severely constrained because of the sensitivity of this high-magnification event to binaries with projected separation $\lesssim 200$ au. However, it is only a small fraction of possible wide separation binary companions that will have a separation from the source that is consistent with the light-curve prediction for the lens. An analysis following the method of Koshimoto et al. (2020) indicates a probability of $<0.1\%$ that the star we identify as the lens star is actually a binary companion to the lens star.

6. Lens Properties

In order to obtain good sampling of light-curve model parameters that are consistent with our photometric constraints and astrometry, we apply the following constraints, along with Galactic model constraints, when summing over our light-curve modeling MCMC results to determine the final parameters. The proper motion vectors $\mu_{\mathrm{rel,H},l}$ and $\mu_{\mathrm{rel,H},b}$ are constrained to have the values and error bars from the bottom row of Table 4, and the lens magnitudes are constrained to be $K_{\mathrm{L}} = 18.93 \pm 0.08$ and $H_{\mathrm{L}} = 19.08 \pm 0.11$. The $\mu_{\mathrm{rel,H}}$ constraints are applied to the Galactic model, and the lens magnitude constraints are applied when combining the MCMC light-curve model results with the Galactic model. The lens magnitude constraints

require the use of a mass–luminosity relation. We built an empirical mass–luminosity relation following the method presented in Bennett et al. (2018). This relation is a combination of mass–luminosity relations for different mass ranges. For $M_L \geqslant 0.66\,M_\odot$, $0.54\,M_\odot \geqslant M_L \geqslant 0.12\,M_\odot$, and $0.10\,M_\odot \geqslant M_L \geqslant 0.07\,M_\odot$, we use the relations of Henry & McCarthy (1993), Delfosse et al. (2000), and Henry et al. (1999), respectively. In between these mass ranges, we linearly interpolate between the two relations used on the boundaries. That is, we interpolate between the Henry & McCarthy (1993) and the Delfosse et al. (2000) relations for $0.66\,M_\odot > M_L > 0.54\,M_\odot$, and we interpolate between the Delfosse et al. (2000) and Henry et al. (1999) relations for $0.12\,M_\odot > M_L > 0.10\,M_\odot$. When using these relations, we assume a 0.05 magnitude uncertainty.

For the mass–luminosity relations, we must also consider the foreground extinction. At a Galactic latitude of $b = -4°.7009$, most of the dust is likely to be in the foreground of the lens unless it is very close to us. We quantify this by relating the extinction of the foreground of the lens to the extinction in the foreground of the source. Assuming a dust scale height of $h_{\rm dust} = 0.10 \pm 0.02$ kpc, we have

$$A_{i,L} = \frac{1 - e^{-|D_L(\sin b)/h_{\rm dust}|}}{1 - e^{-|D_S(\sin b)/h_{\rm dust}|}} A_{i,S}, \qquad (6)$$

where the index i refers to the passband: V, I, H, or K.

These dereddened magnitudes can be used to determine the angular source radius, θ_*. With the source magnitudes that we have measured, the most precise determination of θ_* comes from the $(V - I)$, I relation. We use

$$\begin{aligned}
\log_{10}&[2\theta_*/(1{\rm mas})] \\
&= 0.501414 + 0.419685(V - I)_{s0} - 0.2\,I_{s0}, \qquad (7)
\end{aligned}$$

which comes from the Boyajian et al. (2014) analysis, but with the color range optimized for the needs of microlensing surveys (Bhattacharya et al. 2016).

We apply the H- and K-band mass–luminosity relations to each of the models in our Markov Chains using the mass determined by the first expression of Equation (1), using the θ_E value determined from $\theta_E = \theta_* t_E / t_*$, where t_E and t_* are light-curve parameters given in Table 1. We can then use the Keck H- and K-band measurements of the lens star brightness from Table 3 to constrain the lens brightness including both the observational uncertainties listed in Table 3 and the 0.05 mag theoretical uncertainty that we assumed for our empirical H- and K-band mass–luminosity relations. We solve the first expression of Equation (1) along with the mass–luminosity relations. While solving, we assume the source distance $D_S = 7.76^{+0.98}_{-0.87}$ kpc. This yields the host star mass and the lens distance as shown in Figure 4.

However, for our final values, we solved for the host mass and distance using a different method.

To solve for the planetary system parameters, we use the same two parts: first expression of Equation (1) and mass–luminosity relations. But this time, we sum over our MCMC results using the Galactic model employed by Bennett et al. (2014) as a prior, weighted by the microlensing rate and the measured $\mu_{\rm rel,H}$ values given in Table 4. The results of our final sum over the Markov Chain light-curve models are given in Table 5 and Figure 5. This table gives the mean and rms uncertainty plus the central 95.4% confidence interval range for each parameter except the 3D separation, a_{3D}, where we give
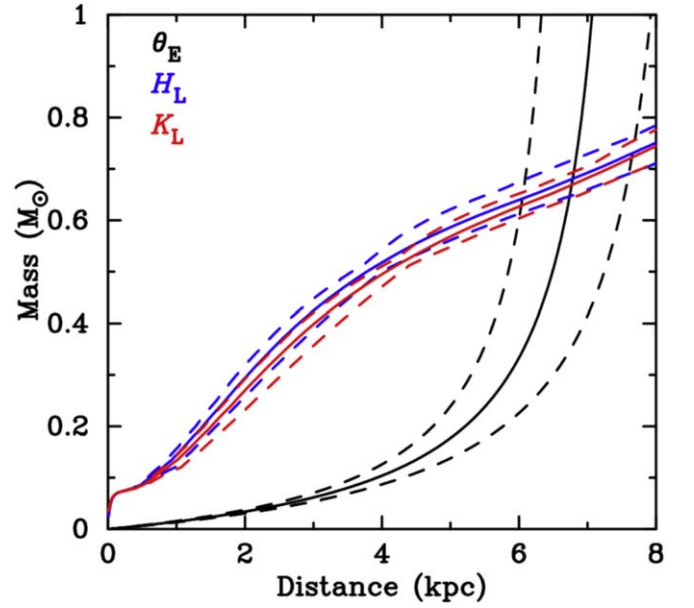

Figure 4. The H_L and K_L brightnesses of lens yields the mass–distance relations shown in the plot. These mass–distance relations intersect the mass–distance relation obtained from the Einstein radius obtained from the light curve. The intersection of these different mass–distance relations yields the mass and distance to the lens system. It is also to be noted that the mass–distance relations from the H_L and K_L brightnesses both independently intersect the θ_E mass–distance relation at the same place. This shows that the mass measurements made independently from two different passbands are consistent.

the median and the central 68.3% confidence interval instead of the mean and rms. The lens flux and the $\mu_{\rm rel,H}$ measurements exclude most of the masses and distances for this planetary system that were compatible with Bayesian analysis and MCMC light-curve models without any $\mu_{\rm rel,H}$ or lens brightness constraints. The host mass is measured to be $M_{\rm host} = 0.69 \pm 0.04\,M_\odot$, a K-dwarf star, orbited by a super-Jupiter-mass planet, $M_{\rm Jup} = 1.71 \pm 0.27$. The separation distribution is bimodal with the close and wide solutions yielding $a_\perp = 0.79 \pm 0.10$ au and $a_\perp = 5.9 \pm 0.7$ au, respectively. This analysis also implies a lens system distance of $D_L = 6.97 \pm 0.77$ kpc. These results show that the planet is slightly less than twice the mass of Jupiter orbiting a K-dwarf that is very likely to be in the bulge.

Figure 5 shows the posterior distributions of the planet and host masses, their 3D separation (assuming a random orientation), and the distance to the planetary lens system. The blue histograms in this figure show the results based on only the $\theta_E = \theta_* t_E / t_*$ measurement from the light curve, and the Galactic prior. This calculation also makes the assumption that possible host stars of any mass are equally likely to host a planet of the observed mass ratio, $q = (2.34 \pm 0.34) \times 10^{-3}$ and separation, $s = 0.365 \pm 0.024$ or $s = 2.72 \pm 0.14$ (for the degenerate close and wide models). The red histograms are the results after including the constraints from our Keck H- and K-band AO images. These show that the host mass is near the top of the range predicted by the analysis prior to the Keck constraints. In fact, the host mass is in the 93rd percentile of the predicted distribution.

The Keck observations have constrained the host star K- and H-band magnitudes, as indicated in Table 3, and Table 5 also gives the inferred host star V- and I-band magnitudes. When comparing these results with the analysis in the discovery
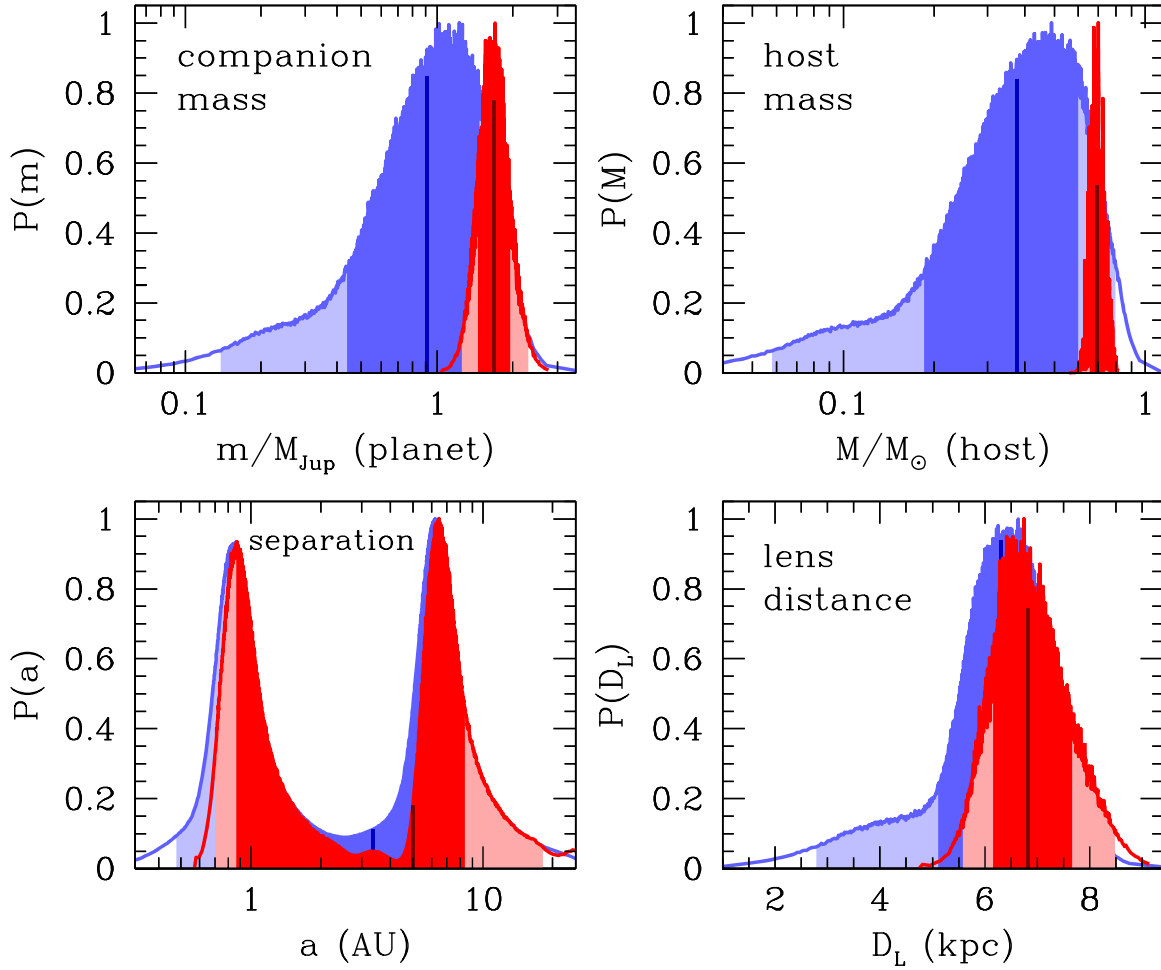
Figure 5. The Bayesian posterior probability distributions for the planetary companion mass, host mass, their separation, and the distance to the lens system are shown with only light-curve constraints in blue and with the additional constraints from our Keck and HST follow-up observations in red. The central 68.3% of the distributions is shaded in darker colors (dark red and dark blue), and the remaining central 95.4% of the distributions is shaded in lighter colors. The vertical black line marks the median of the probability distribution of the respective parameters.

Table 5
Measurement of Planetary System Parameters Including the Lens Flux Constraints

Parameter	Units	Values and rms	2σ Range
Angular Einstein Radius, θ_E	mas	0.322 ± 0.010	0.303–0.342
Geocentric lens-source relative proper motion, $\mu_{\text{rel, G}}$	mas yr^{-1}	8.77 ± 0.13	8.50–9.04
Host star mass, M_{host}	$M_{\odot}$	0.69 ± 0.04	0.62–0.78
Planet mass, m_p	M_{Jup}	1.70 ± 0.26	1.26–2.31
Host star–planet 2D separation, $a_{\perp\text{close}}$	au	0.79 ± 0.10	0.6–1.0
Host star–planet 2D separation, $a_{\perp\text{wide}}$	au	5.9 ± 0.7	4.7–7.7
Lens distance, D_L	kpc	6.89 ± 0.77	5.57–8.48
Lens magnitude, I_L		21.24 ± 0.10	21.07–21.53
Lens magnitude, V_L		23.47 ± 0.21	23.08–24.01

Note. The star–planet 2D separations are different for close and wide light-curve models and are listed as $a_{\perp\text{close}}$ and $a_{\perp\text{wide}}$, respectively.

paper, we find that they are not entirely consistent. Dong et al. (2009) claim a limit on the ratio brightness of a star blended with the source to the flux from the source to be $f_b/f_s < 0.05$, where f_b and f_s are the fluxes of the blend and source stars, respectively. This blend flux is expected to include both the planetary host star and any other star that might be unresolved from the source at the time of the event. However, it is also

important to consider the fact that the apparent smooth background light in seeing-limited images of the Galactic bulge contains a considerable amount of unresolved starlight. So, the background light is mottled rather than smooth, and because of this, it is possible to have negative blend fluxes. Dong et al. (2009) make some allowances for this, but they apparently are not enough. Gould et al. (2020) present a more

rigorous solution to this issue. We have found $I_S = 18.39$ (Table 1) and $I_L = 21.24 \pm 0.13$ (Table 5), which implies an I-band value of $f_b/f_s = 0.073 \pm 0.007$. This is a $\sim 3\sigma$ discrepancy, but we should note that the revised MOA photometry has changed the situation slightly. The improved photometry reduces the Einstein radius crossing time from $t_E 14.33$ days to $t_E 13.39$ days, a reduction of 7%. Since the product $f_s t_E$ is an approximate invariant, this should be reflected in an increase in the brightness of the source by $\sim 7\%$. The reasoning behind Dong et al.'s (2009) claimed limit of $f_b/f_s < 0.05$ is not entirely clear, but it is clear their method would result in a tighter limit than the Dong et al. (2009) claimed limit of $f_b/f_s < 0.05$. On the other hand, there may be some uncertainty due to the conversion from measured H- and K-band magnitudes indeed relying upon extinction laws and empirical color–color relations. The conversion to constraints on the lens mass depends on mass–luminosity relations and the source distance, D_S. Dong et al. (2009) claim a limit of $M_{host} < 0.75 M_\odot$ without specifying which mass–luminosity relation or D_S are used. This is consistent with the 1σ range of $0.65 M_\odot < M_{host} < 0.73 M_\odot$, but not quite consistent with the top end of the $0.62 M_\odot < M_{host} < 0.78 M_\odot$ 2σ range determination. This is similar to the overly strict lens star limits for MOA-2013-BLG-220L (Yee et al. 2014; Vandorou et al. 2020).

7. Discussion and Conclusions

We have detected the planetary host star for microlensing event MOA-2007-BLG-400, and determined that the planetary lens system consists of a gas giant of slightly less than twice Jupiter's mass orbiting a K-dwarf star. In our high angular resolution follow-up observations from Keck, we have resolved the source and the lens to a separation of ~ 96 mas in the K and H bands, enabling us to accurately measure their fluxes and relative proper motion. We employed improved photometry methods to the majority of the light-curve data for this event (Bond et al. 2017), and this slightly decreased the Einstein radius crossing time, t_E, and mass ratio, q, parameters. Using this improved photometry and constraints from the Keck observations, we found that the host star is a K-dwarf located in, or very close to, the Galactic bulge. Due to the close-wide light-curve degeneracy, we cannot be certain if the planet has a projected separation of $a_\perp = 0.79 \pm 0.10$ au or $a_\perp = 5.9 \pm 0.7$ au. The snow line of the host star is likely to be at $\sim 2.7 M_{host}/M_\odot \simeq 1.86$ au (Kennedy & Kenyon 2008). The close solution would likely put this gas giant planet well inside the snow line and near the habitable zone of the host star, while the wide separation solution would put it well beyond the snow line, where most microlens planets are found.

There are very few microlens planets detected so far inside the snow line of the host star, but because of the close-wide degeneracy, we do not know if the planet MOA-2007-BLG-400Lb lies inside or outside of the snow line. Suzuki et al. (2016) shows the planet detection sensitivity for a mass ratio of 2.34×10^{-3} of MOA survey spans a wide range of separations. The radial velocity technique has regularly detected Jovian planets at separations of ~ 1.0 au, so we should expect that gas giant planets with the projected, 2D separation of the close solution, 0.6–1.0 au, are relatively common. Thus, we have no reason to think that the close solution would be disfavored on the basis of radial velocity survey results. In the future, if we know about planet occurrence rates at $\lesssim 1$ au from radial velocity and transits, we may be able to use this information to

statistically break the close-wide degeneracy for such gas giant planets. That is, if we have a sample of close-wide degenerate events, we may be able to use it to determine what percentage of the close-wide degenerate events are actually in the close configuration.

One of the most interesting features of Figure 5 is that the host mass is much more massive than the prediction from the Bayesian analysis, which assumes that stars of all masses are equally likely to host planets. The measured mass is at the 93rd percentile of the predicted distribution, shown as the blue histogram. This is nearly identical to the situation with MOA-2013-BLG-220L (Vandorou et al. 2020), which has a mass ratio of $q = (3.26 \pm 0.04) \times 10^{-3}$, which compares to the mass ratio of $q = (2.34 \pm 0.44) \times 10^{-3}$ for MOA-2007-BLG-400L. Both lens systems reside in or very near to the Galactic bulge, and both are in the 93rd percentile of the predicted mass distribution, if we assume that all stars are equally likely to host planets of the observed mass ratios. This shows the importance of the mass measurements over the Bayesian mass estimates that are published in most of the microlensing planet discovery papers.

MOA-2007-BLG-400 is the sixth planetary microlensing event published by our group with a direct measurement of the separation between the lens and source stars. The others are OGLE-2005-BLG-071 (Bennett et al. 2020a), OGLE-2005-BLG-169 (Batista et al. 2015; Bennett et al. 2015), MOA-2009-BLG-319 (Terry et al. 2021), OGLE-2012-BLG-0950 (Bhattacharya et al. 2018), and MOA-2013-BLG-220 (Vandorou et al. 2020). Of these events, only the OGLE-2005-BLG-071L lens star has a smaller mass than the median prediction from a Bayesian analysis, which assumes that the planet hosting probability is independent of host star mass. The probability of having only zero or one mass measurements below the median prediction is 11% (as determined from the binomial distribution). One might be concerned that this comparison may be compromised by "publication bias," which would be the case if events with lens star detections are published while events with only upper limits on the lens star brightness are not. Fortunately, this published sample can be defined without reference to the lens star detection. It consists of events with $\theta_E > 0.8$ mas or lens-source separations of > 60 mas at the time of the observations. There are some planetary microlensing events satisfying these conditions that are not yet published, but these are not yet published due to reasons unrelated to the host star mass dependence (such as analysis complications due to a diffraction spike from a nearby bright star). Thus, this small sample is not affected by publication bias, and it suggests that more massive host stars are more likely to host microlens planets of a fixed mass ratio. Earlier exoplanet results from radial velocities seem to support this idea (Johnson et al. 2007, 2010), but these comparisons were at fixed planetary mass, rather than fixed mass ratio. Also, 90% of these radial velocity detected planets had super-Jupiter-mass ratios, and only about 60% of the Johnson et al. (2010) sample is in orbits > 0.6 au where microlensing has significant sensitivity to Jovian planets. So, the microlensing results focus more on wider orbit planets and extend down to lower masses. Of course, we do need a larger sample of microlens planets with host star mass measurements to resolve this issue, and this is the goal of our NASA Keck KSMS and HST observing programs.

This event is the first event to be published with lens detection in a microlensing system where the lens is ~10 times fainter than the source star. It is much easier to detect the lens star when the lens and source are of comparable brightness and are separated by $\gtrsim$30 mas. This lens host is also one of the faintest host stars detected using Keck AO (Blackman 2020; Terry et al. 2021). Our detection of the lens in a single high-S/N image with an FWHM of 94 mas in 2013, when the lens-source separation was ~50 mas, implies that a full set of ~20 high-S/N images would have enabled the detection of the lens star at a separation of 0.53 FWHM, with a contrast ratio of 10:1. We estimate that if we had managed to get more good-quality S/N images in 2013, it would have been possible to detect the lens. It is clear that as the contrast between lens and source increases, it becomes increasingly harder to detect the lens. The Roman Galactic Exoplanet Survey will have ~4.5 yr difference between the first and the last epoch. Hence, the lens detection of an event with similar lens-source brightness contrast as MOA-2007-BLG-400 and a lens-source separation of ~40 mas in 4.5 yr might be challenging, if it were not for the much more stable Roman PSFs and the many thousands of images that the Roman Galactic Exoplanet Survey will obtain for each event. However, events with much smaller lens-source flux ratios might require follow-up observations with Extremely Large Telescopes equipped with Laser Guide Star AO systems and following the same image analysis methods discussed by Bhattacharya et al. (2019a).

This planetary event is part of the Suzuki et al. (2016) statistical sample of 30 planets found by the MOA microlensing survey and previous smaller statistical studies. This study and a follow-up analysis (Suzuki et al. 2018) examine the exoplanet-host mass ratio function, which is readily available from the light-curve models, but they do not examine how the exoplanet distribution depends on host mass. This event increases the number of planets in this sample with mass measurements or upper limits to 12, and we have high angular resolution data for many more of these events that are in the process of being analyzed. Suzuki et al. (2018) showed that the observational occurrence rate shows no deficit of intermediate-mass giant planets, with mass ratios in the range $10^{-4} < q < 4 \times 10^{-4}$. This contradicts a prediction based on the runaway gas accretion process, which predicted a "desert" in the distribution of exoplanets with these mass ratios (Ida & Lin 2004). Three-dimensional hydrodynamic simulations of gas giant planet formation seem to yield a similar result (Szulágyi et al. 2014, 2016). However, the results of Suzuki et al. (2016) do not include any dependence on host star mass, and this is what we aim to correct with our high angular resolution follow-up observation program. In particular, we plan to determine the exoplanet mass ratio function as a function of the host star mass, and to investigate whether or not the exoplanet mass function provides a simpler description of exoplanet demographics than the mass ratio function does.

We expect that high angular resolution follow-up observations combined with microlensing parallax measurements will be able to measure or significantly constrain the host masses for 80% of the Suzuki et al. (2016) sample, and we expect to expand this sample to include some planets recently found in the 2006 season data (Bennett et al. 2012, 2020b; Kondo et al. 2019), as well as events that occurred more recently than 2012.

ORCID iDs

David P. Bennett https://orcid.org/0000-0001-8043-8413
Jean Philippe Beaulieu https://orcid.org/0000-0003-0014-3354
Naoki Koshimoto https://orcid.org/0000-0003-2302-9562
Jessica R. Lu https://orcid.org/0000-0001-9611-0009
Joshua W. Blackman https://orcid.org/0000-0001-5860-1157
Aikaterini Vandorou https://orcid.org/0000-0002-9881-4760
Virginie Batista https://orcid.org/0000-0002-9782-0333
Andrew A. Cole https://orcid.org/0000-0003-0303-3855
Akihiko Fukui https://orcid.org/0000-0002-4909-5763
Calen B. Henderson https://orcid.org/0000-0001-8877-9060
Clément Ranc https://orcid.org/0000-0003-2388-4534

References

Anderson, J., & Bedin, L. R. 2010, PASP, 122, 895
Batista, V., Beaulieu, J.-P., Bennett, D. P., et al. 2015, ApJ, 808, 170
Batista, V., Beaulieu, J.-P., Gould, A., et al. 2014, ApJ, 780, 54
Beaulieu, J. P., Batista, V., Bennett, D. P., et al. 2017, AJ, 155, 78
Bennett, D. 2018, Keck Observatory Archive, N02, 124
Bennett, D. P. 2008, in Exoplanets, ed. John Mason (Berlin: Springer)
Bennett, D. P. 2010, ApJ, 716, 1408
Bennett, D. P., Akeson, R., Alibert, Y., et al. 2019, BAAS, 51, 505
Bennett, D. P., Anderson, J., Beaulieu, J.-P., et al. 2010a, arXiv:1012.4486
Bennett, D. P., Anderson, J., Bond, I. A., Udalski, A., & Gould, A. 2006, ApJL, 647, L171
Bennett, D. P., Anderson, J., & Gaudi, B. S. 2007, ApJ, 660, 781
Bennett, D. P., Batista, V., Bond, I. A., et al. 2014, ApJ, 785, 155
Bennett, D. P., Bhattacharya, A., Anderson, J., et al. 2015, ApJ, 808, 169B
Bennett, D. P., Bhattacharya, A., Beaulieu, J.-P., et al. 2020a, AJ, 159, 68
Bennett, D. P., Rhie, S., et al. 2010b, ApJ, 713, 837
Bennett, D. P., & Rhie, S. H. 1996, ApJ, 472, 660
Bennett, D. P., & Rhie, S. H. 2002, ApJ, 574, 985
Bennett, D. P., Sumi, T., Bond, I. A., et al. 2012, ApJ, 757, 119
Bennett, D. P., Udalski, A., Bond, I. A., et al. 2018, AJ, 156, 113

Bennett, D. P., Udalski, A., Bond, I. A., et al. 2020b, AJ, 160, 72
Bertin, E., & Arnouts, S. 1996, A&AS, 117, 393
Bertin, E., Mellier, Y., Radovich, M., et al. 2002, in ASP Conf. Ser. 281, The TERAPIX Pipeline (San Francisco, CA: ASP), 228
Bhattacharya, A., Akeson, R., Anderson, J., et al. 2019a, BAAS, 51, 520
Bhattacharya, A., Anderson, J., Beaulieu, J.-P., et al. 2019b, HST Proposal, 26, 15690
Bhattacharya, A., Beaulieu, J.-P., Bennett, D. P., et al. 2018, AJ, 156, 289
Bhattacharya, A., Bennett, D. P., Anderson, J., et al. 2017, AJ, 154, 2
Bhattacharya, A., Bennett, D. P., Bond, I. A., et al. 2016, AJ, 152, 140
Blackman, J. 2020, Sci, submitted
Bond, I. A., Abe, F., Dodd, R. J., et al. 2001, MNRAS, 327, 868
Bond, I. A., Bennett, D. P., Sumi, T., et al. 2017, MNRAS, 469, 2434
Borucki, W. J., Koch, D. G., Basri, G., et al. 2011, ApJ, 736, 19
Boyajian, T. S., van Belle, G., & von Braun, K. 2014, AJ, 147, 47
Cardelli, J. A., Clayton, G. C., & Mathis, J. A. 1989, ApJ, 345, 245C
Clanton, C., & Gaudi, B. S. 2014a, ApJ, 791, 90
Clanton, C., & Gaudi, B. S. 2014b, ApJ, 791, 91
Dang, L., Calchi Novati, S., Carey, S., et al. 2020, MNRAS, 497, 5309
Delfosse, X., Forveille, T., Ségransan, D., et al. 2000, A&A, 364, 217
Dong, S., Bond, I. A., Gould, A., et al. 2009, ApJ, 698, 1826
Fernandes, R. B., Mulders, G. D., Pascucci, I., et al. 2019, ApJ, 874, 81
Gaudi, B. S. 2012, ARA&A, 50, 411
Gaudi, B. S., Bennett, D. P., Udalski, A., et al. 2008, Sci, 319, 927
Gould, A., Bennett, D. P., & Alves, D. R. 2004, ApJ, 614, 404
Gould, A., & Loeb, A. 1992, ApJ, 396, 104G
Gould, A., Ryu, Y.-H., Calchi Novati, S., et al. 2020, JKAS, 53, 9
Henry, T. J., Franz, O. G., Wasserman, L. H., et al. 1999, ApJ, 512, 864
Henry, T. J., & McCarthy, D. W., Jr. 1993, AJ, 106, 773
Ida, S., & Lin, D. N. C. 2004, ApJ, 604, 388
Johnson, J. A., Aller, K. M., Howard, A. W., & Crepp, J. R. 2010, PASP, 122, 905
Johnson, J. A., Butler, R. P., Marcy, G. W., et al. 2007, ApJ, 670, 833
Jung, Y. K., Gould, A., Zang, W., et al. 2019, AJ, 157, 72
Kennedy, G. M., & Kenyon, S. J. 2008, ApJ, 673, 502
Kenyon, S. J., & Hartmann, L. 1995, ApJSS, 101, 117
Kervella, P., Thévenin, F., Di Folco, E., & Ségransan, D. 2004, A&A, 426, 297
Kondo, I., Sumi, T., Bennett, D. P., et al. 2019, AJ, 158, 224

Koshimoto, N., & Bennett, D. 2020, AJ, 159, 268
Koshimoto, N., Bennett, D. P., & Suzuki, D. 2020, AJ, 159, 268
Lissauer, J. J. 1993, ARA&A, 31, 129
Lu, J. R. 2008, PhD thesis, UCLA
Minniti, D., Lucas, P. W., Emerson, J. P., et al. 2010, NewA, 15, 433
Mordasini, C., Alibert, Y., & Benz, W. 2009, A&A, 501, 1139
Muraki, Y., Han, C., Bennett, D. P., et al. 2011, ApJ, 741, 22
Nataf, D. M., Gould, A., Fouqué, P., et al. 2013, ApJ, 769, 88
Pollack, J. B., Hubickyj, O., Bodenheimer, P., et al. 1996, Icar, 124, 62
Quenouille, M. H. 1949, Ann. Math. Stat., 20, 355
Quenouille, M. H. 1956, Biometrika, 43, 353
Rhie, S. H., Becker, A. C., Bennett, D. P., et al. 1999, ApJ, 522, 1037
Schechter, P. L., Mateo, M., & Saha, A. 1993, PASP, 105, 1342
Service, M., Lu, J. R., Campbell, R., et al. 2016, PASP, 128, 095004
Spergel, D., Gehrels, N., Baltay, C., et al. 2015, arXiv:1503.03757
Stetson, P. B. 1987, PASP, 99, 191S
Street, R. A., Udalski, A., Calchi Novati, S., et al. 2016, ApJ, 819, 93
Sumi, T., Bennett, D. P., Bond, I. A., et al. 2010, ApJ, 710, 1641
Sumi, T., Udalski, A., Bennett, D. P., et al. 2016, ApJ, 825, 112
Suzuki, D., Bennett, D. P., Ida, S., et al. 2018, ApJL, 869, L34
Suzuki, D., Bennett, D. P., Sumi, T., et al. 2016, ApJ, 833, 2
Szulágyi, J., Masset, F., Lega, E., et al. 2016, MNRAS, 460, 2853
Szulágyi, J., Morbidelli, A., Crida, A., et al. 2014, ApJ, 782, 65
Szymański, M. K., Udalski, A., Soszyński, I., et al. 2011, AcA, 61, 83
Terry, S. K., Bhattacharya, A., Bennett, D. P., et al. 2021, AJ, 161, 54
Thompson, S. E., Coughlin, J. L., Hoffman, K., et al. 2018, ApJS, 235, 38
Tierney, L., & Mira, A. 1999, Stat. Med., 18, 2507
Tukey, J. W. 1958, Ann. Math. Stat., 29, 614
Udalski, A., Ryu, Y.-H., Sajadian, S., et al. 2018, AcA, 68, 1
Udalski, A., Yee, J. C., Gould, A., et al. 2015, ApJ, 799, 237
Vandorou, A., Bennett, D. P., Beaulieu, J.-P., et al. 2020, AJ, 160, 121
Wittenmyer, R. A., Wang, S., Horner, J., et al. 2020, MNRAS, 492, 377
Wizinowich, P., Action, S., Shelton, C., et al. 2000, PASP, 112, 315
Yee, J. C., Han, C., Gould, A., et al. 2014, ApJ, 790, 14
Yee, J. C., Shvartzvald, Y., Gal-Yam, A., et al. 2012, ApJ, 755, 102
Yelda, S., Lu, J. R., Ghez, A. M., et al. 2010, ApJ, 725, 331
Yoo, J., Depoy, D. L., Gal-Yam, A., et al. 2004, ApJ, 603, 139